Conformation of Valine Side Chains in Ribonuclease T_1 Determined by NMR Studies of Homonuclear and Heteronuclear ^3J Coupling Constants†

Yasmin Karimi-Nejad, Jürgen M. Schmidt, and Heinz Rüterjans*

Institut für Biophysikalische Chemie, Johann Wolfgang Goethe-Universität, Frankfurt, Biozentrum Niederursel, Marie-Curie-Str. 9, D-60439 Frankfurt/Main, Germany

Harald Schwalbe and Christian Griesinger

Institut für Organische Chemie, Johann Wolfgang Goethe-Universität, Frankfurt, Marie-Curie-Str. 11, D-60439 Frankfurt/Main, Germany

Received November 16, 1993●

ABSTRACT: A conformational analysis of the valine side chains of ribonuclease T_1 (RNase T_1) was performed using NMR spectroscopy, in particular homonuclear (^{1}H,^{1}H and ^{13}C,^{13}C) and heteronuclear (^{1}H,^{15}N and ^{1}H,^{13}C) vicinal spin–spin coupling constants as obtained from E.COSY-type NMR experiments. The coupling constants related to the χ_1 dihedral angle in valine, $^3J_{H\alpha H\beta}$, $^3J_{NH\beta}$, $^3J_{C'H\beta}$, $^3J_{H\alpha C\gamma 1}$, $^3J_{H\alpha C\gamma 2}$, $^3J_{C'C\gamma 1}$, and $^3J_{C'C\gamma 2}$, were evaluated in a quantitative manner. The analysis of ^3J data allowed for the stereospecific assignment of the valine methyl resonances. On the basis of various models for motional averaging of coupling constants, a fit of the torsion angles χ_1 to a set of the experimental ^3J coupling constants ($^3J_{H\alpha H\beta}$, $^3J_{NH\beta}$, $^3J_{C'H\beta}$) was carried out. The resulting side-chain conformations were examined with respect to NOE distance informations. Single rotameric states emerged for Val16, Val67, Val79, and Val101, while conformational equilibria between staggered rotamers were found for Val33 and Val78. Using a different model approach, Val52 and Val89 are also likely to exhibit unimodal χ_1 angle distributions. The analysis was found to depend critically on the set of Karplus parameters used. Except for Val52 and Val78, the predominant rotamers obtained from ^3J coupling informations agree with the conformation in the crystal structure of ribonuclease T_1 (Martinez-Oyanedel et al., 1991).

Vicinal spin–spin coupling constants have found widespread use in the conformational analysis of amino acids and peptides (Kopple et al., 1973; Mádi et al., 1990). For proteins, the use of coupling constants has so far been limited to a more qualitative dihedral angle evaluation (Nagayama & Wüthrich, 1981; Hyberts et al., 1987; Smith et al., 1991). The limitation was mainly due to difficulties in the precise determination of coupling constants owing to the large line widths and to the overlap of resonances typically encountered in protein spectra. This problem has been recently solved by a variety of heteronuclear NMR techniques (Montelione et al., 1989; Wider et al., 1989; Sørensen, 1990; Wagner et al., 1991; Griesinger & Eggenberger, 1992; Eggenberger et al., 1992a) based on the E.COSY[1] principle (Griesinger et al., 1985, 1986, 1987). Sensitivity problems in the determination of heteronuclear couplings are now overcome with the availability of isotopically labeled samples.

Karplus parameters (Karplus, 1959, 1963), which relate ^3J coupling constants to dihedral angles, are known for most of the spin pairs relevant to the conformational analysis of proteins (Bystrov, 1976). Since Karplus relations are not single-valued functions, delivering up to four different dihedral angle values for a given ^3J value, a set of homo- and heteronuclear coupling constants must be determined to unambiguously characterize a dihedral angle.

The interpretation of vicinal coupling constants in terms of a unique dihedral angle is hampered by conformational mobility, as coupling constants may be time averages over multiple conformations (Pople, 1958; Kessler et al., 1988). In the case of amino acid side chains in peptides, the Pachler analysis (Pachler, 1963, 1964) has been successfully used to interpret motionally averaged coupling constants in terms of conformational equilibria between staggered rotamers about the side-chain dihedral angle χ_1 (Kessler et al., 1987). These particular side-chain conformations are depicted for L-valine in Figure 1. For proteins, the staggered rotamer model might be inappropriate for the following reasons: First, nonstaggered rotamers may occur due to a shifted torsional potential minimum which arises from structural interactions in the protein matrix, e.g., from hydrogen bonds (Gelin & Karplus, 1979). Indeed, statistical studies of X-ray protein structures (Janin et al., 1978; Ponder & Richards, 1987) indicate that crystallographic χ_1 values often deviate from the ideal staggered conformations. According to these analyses, even eclipsed rotameric states do occur. Second, a limitation to discrete rotamers may not be correct, considering the results of relaxation studies (Richarz et al., 1980; Clore et al., 1990; Palmer et al., 1991; Nicholson et al., 1992) and of MD simulations (Ichiye & Karplus, 1987), indicating a consider-

† H.S. acknowledges a grant from the Fonds der Chemischen Industrie and a Scholarship from a Graduiertenkolleg of the University of Frankfurt. Y.K.-N. gratefully acknowledges a grant from the Graduiertenförderung NRW. This work was supported in part by the Fonds der Chemischen Industrie and by the Deutsche Forschungsgemeinschaft (Gr1211/2-1 and Ru145/8-6).

* Author to whom correspondence should be addressed.

● Abstract published in *Advance ACS Abstracts,* April 1, 1994.

[1] Abbreviations: E.COSY, exclusive correlation spectroscopy; DIPSI, a composite pulse decoupling scheme; GARP, a composite pulse decoupling scheme; HMQC, heteronuclear multiple-quantum coherence; HMBC, heteronuclear multiple bond multiple-quantum coherence; NOE, nuclear Overhauser enhancement; NOESY, nuclear Overhauser enhancement and exchange spectroscopy; RNase T_1, ribonuclease T_1; RSH, quadrature detection scheme according to Ruben, States, and Haberkorn; TPPI, time proportional phase incrementation; TOCSY, total correlation spectroscopy. Enzyme: ribonuclease T_1 [EC 3.1.27.3].

0006-2960/94/0433-5481$04.50/0

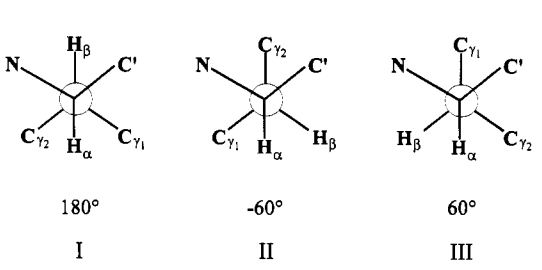

FIGURE 1: Designation of nuclei and χ_1 dihedral angles associated with the three staggered side-chain conformations in L-valine.

able degree of local mobility in the backbone as well as in the side chains of a protein. The observed angular fluctuations often amount to approximately ±15° about a discrete mean dihedral angle.

Distributions of dihedral angles can be readily approximated by uni- or multimodal Gaussian angular-probability functions (Hoch et al., 1985). Recently, a method termed CUPID (Dzakula et al., 1992a,b) has been developed to investigate a continuous probability distribution of rotamers in amino acids leading to angle-probability profiles based on a combination of NOE and ^3J coupling information. In a different approach, coupling constants are used as time-dependent torsion angle restraints in MD simulations (Torda et al., 1993) to allow for conformational flexibility. However, to unambiguously characterize local side-chain conformations, both of these methods utilize information in addition to ^3J data, e.g., crystallographic coordinates or NOE distances. Therefore, it seems useful to develop a methodology to reach at torsional angles by applying exclusively a set of vicinal coupling constants.

In this paper, we report on a quantitative evaluation of valine side-chain conformations in ribonuclease T_1 which is based entirely on ^3J coupling constants. Seven out of nine possible vicinal coupling constants related to the dihedral angle χ_1 of valine side chains have been measured, including $^3J_{H\alpha H\beta}$, $^3J_{NH\beta}$, $^3J_{C'H\beta}$, $^3J_{H\alpha C\gamma 1}$, $^3J_{H\alpha C\gamma 2}$, $^3J_{C'C\gamma 1}$, and $^3J_{C'C\gamma 2}$, using E.COSY-type multidimensional heteronuclear NMR techniques. The ^3J data are analyzed with respect to different models for the conformational dynamics of the side chain. In this study, NOE distance information is disregarded in the analysis to explore the feasibility and limits of such an approach. However, the conformations obtained from J coupling data are examined with respect to consistency with NOE data. The results are also compared with the crystal structure of ribonuclease T_1 (Martinez-Oyanedel et al., 1991).

MATERIALS AND METHODS

Ribonuclease T_1 (for a review, see Pace et al., 1991), a small fungal enzyme of 104 amino acids, has been studied in solution by multidimensional ^{1}H NMR (Hoffmann & Rüterjans, 1988), ^{15}N NMR (Schmidt et al., 1991), and ^{13}C NMR spectroscopy (Weisemann & Rüterjans, unpublished). A refined NMR solution structure (Karimi-Nejad et al., 1992) was obtained from distance geometry methods. The crystal structure of RNase T_1 is known to a resolution of 1.5 Å (Martinez-Oyanedel et al., 1991).

Sample Preparation. Uniformly ^{15}N-labeled RNase T_1 was isolated and purified from the recombinant *Escherichia coli* strain DHα/pA2T1 as reported previously (Quaas et al., 1988a,b). For the preparation of ^{13}C,^{15}N-labeled RNase T_1, a M9 minimal medium with uniformly ^{13}C-labeled glucose as the sole carbon source was used (Thüring & Rüterjans, unpublished). The sample of ^{15}N-labeled RNase T_1 used in the 3D ^{1}H,^{15}N-HMQC-NOESY experiment contained 3.5 mM protein dissolved in 90% H_2O/10% D_2O at pH 5.5. For the ^{13}C-correlation experiments, the protein was dissolved in 100% D_2O at a concentration of 2.0 mM and at pH 5.5.

Acquisition and Processing of NMR Data. The NMR spectra were recorded at 308 K on a Bruker AMX-600 spectrometer. For the excitation of ^{13}C nuclei, a Bruker BLKX-300W broad-band linear amplifier was used. The data were processed using the program FELIX (Hare Research, Inc.).

The 3D ^{1}H,^{15}N-HMQC-NOESY experiment (Figure 2a) for the determination of $^3J_{NH\beta}$ coupling constants was performed according to Wider et al. (1989) with an additional refocussing period Δ inserted before the evolution time t_2 to obtain in-phase multiplets in ω_2 with respect to the $^1J(^{15}N,^1H)$ coupling. To prevent the recovery of the H_2O signal, a composite 180° pulse followed by a homospoil pulse of 5-ms length was applied in the middle of the mixing time τ_m which had a duration of 180 ms. $52(t_1) \times 160(t_2) \times 4096(t_3)$ real points were acquired using TPPI (Marion & Wüthrich, 1983) for phase-sensitive detection in t_1 and t_2 dimensions. The acquisition times were 8.7, 22.2, and 282.2 ms in t_1, t_2, and t_3, respectively; spectral widths in ω_1, ω_2, and ω_3 comprised 1496, 3600, and 7246.4 Hz. A total of 32 scans were collected per t_1,t_2 increment, resulting in a total acquisition time of 137 h. The spectrum was processed using squared sine-bell apodization functions shifted by $\pi/2$, $\pi/3$, and $\pi/3$ in t_1, t_2, and t_3, respectively. Zero-filling was applied to yield $64(\omega_1) \times 512(\omega_2) \times 2048(\omega_3)$ real data points after FT, where only the high-field half of the ω_3 dimension was selected.

The 3D SOFT-HCCH-COSY (Figure 2b) for the determination of $^3J_{C'H\beta}$ coupling constants was carried out using the following parameters (Eggenberger et al., 1992a): Δ = 1.7 ms, Δ′ = 0.95 ms, τ = 7 ms, τ′ = 3.05 ms, the homospoil pulses had a duration of 3 and 2 ms, followed by recovery delays of 3 ms. The parameters had to be adjusted in order to compensate for the chemical-shift evolution during the long aliphatic carbon-selective pulses to avoid phase correction in ω_1 and ω_2. Eight scans were accumulated per t_1,t_2 experiment. TPPI was used for phase-sensitive detection in t_1 and RSH (States et al., 1982) in t_2. A total of 74 real, 126 complex, and 1024 complex points were recorded in t_1, t_2, and t_3. The Gaussian G3 inversion pulses had a duration of 250 μs; Gaussian G4 excitation pulses had a duration of 400 μs. Every other carbon 90° pulse had a time-reversed G4 shape. Proton decoupling during $2(\tau + \tau' - \Delta - \Delta')$ was achieved with DIPSI-2, using a 90° ^{1}H pulse length of 200 μs. Aliphatic carbons were decoupled during acquisition using MLEV-16 expansions of G3 pulses of 500-μs length according to AABB BAAB BBAA ABBA, where A represents a G3 with phase x and B a G3 with phase $-x$ (Eggenberger et al., 1992b). Following Fourier transformation in t_1 and t_3, a mirror-image linear prediction (Zhu & Bax, 1990) was used for t_2 data to increase resolution by extending the FID to 475 complex points after mirror imaging. The mirror-imaged points were then discarded. Squared cosine-weighting functions were applied as a window function prior to FT; the spectrum was zero-filled to yield a final frequency domain data matrix of $1024 \times 512 \times 128$ real points in ω_3, ω_2, and ω_1, respectively, after FT. The total measurement time was 79 h.

The $^3J_{H\alpha H\beta}$ coupling constants were determined from a SOFT-HCCH-E.COSY (Eggenberger et al., 1992a) spectrum (pulse sequence shown in Figure 2c), using identical parameters as for the SOFT-HCCH-COSY except for the small-angle

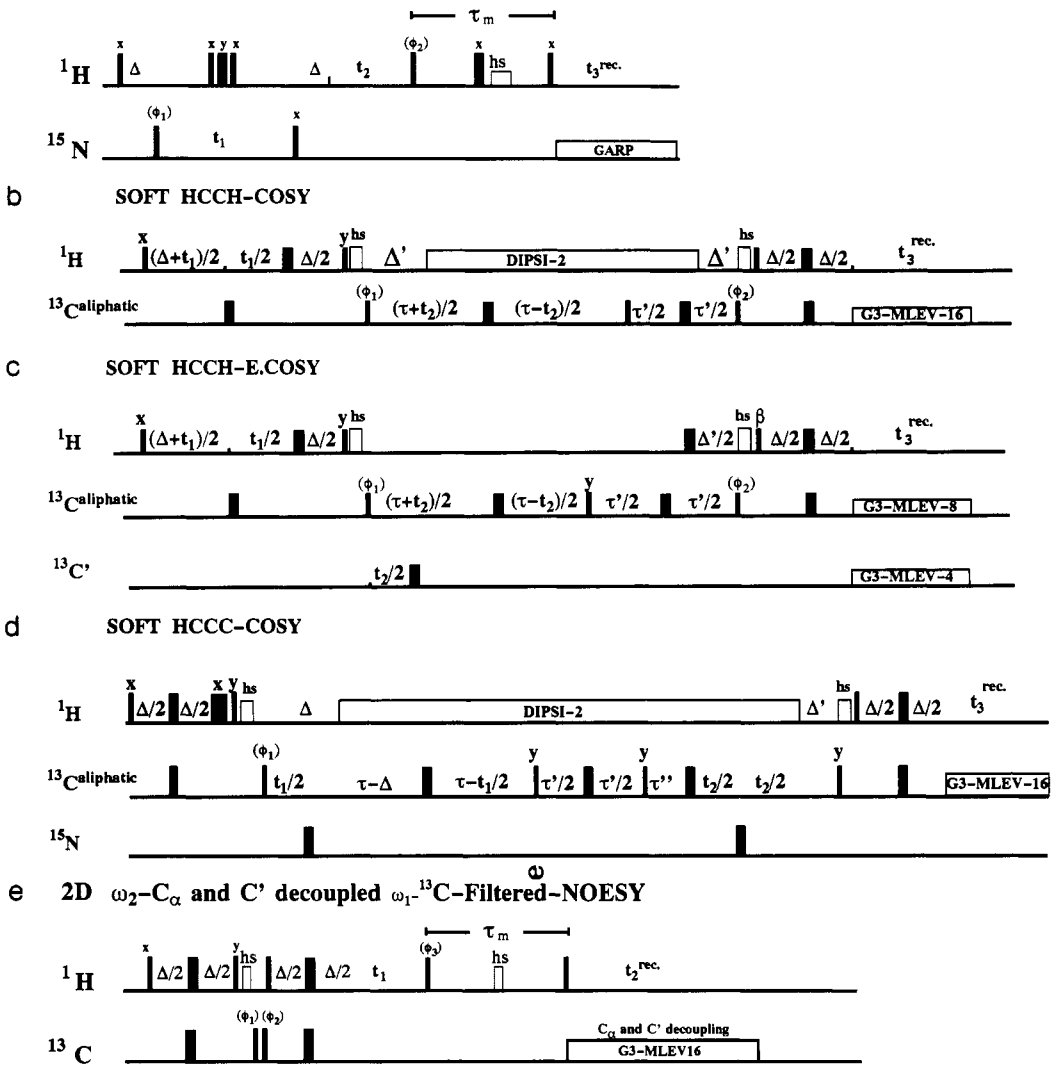

FIGURE 2: Pulse sequences used for the determination of ^3J coupling constants in valine side chains. Unless otherwise stated, narrow and wide bars represent $\pi/2$ and π pulses, respectively. Pulse phases not explicitly given were x; hs denotes a homospoil pulse. (a) The 3D-HMQC-NOESY experiment used for measuring $^3J_{NH\beta}$ coupling constants. Δ is set to $(2\,^1J_{NH})^{-1}$, typically 5.5 ms. The phase cycle is $\phi_1 = x, -x, x, -x$; $\phi_2 = x, x, -x, -x$; rec = $x, -x, -x, x$. (b) Soft HCCH-COSY to determine the $^3J_{C'H\beta}$ coupling constants. $\Delta = (2\,^1J_{CH})^{-1}$, $\Delta' = (4\,^1J_{CH})^{-1}$, $\tau = (2\,^1J_{CC})^{-1}$, $\tau' = (4\,^1J_{CC})^{-1}$, $\phi_1 = x, -x, x, -x$; $\phi_2 = x, x, -x, -x$; rec = $x, -x, -x, x$. (c) Soft HCCH-E.COSY to determine the $^3J_{H\alpha H\beta}$ coupling constants. $\Delta = (2\,^1J_{CH})^{-1}$, $\Delta' = (4\,^1J_{CH})^{-1}$, $\tau = (2\,^1J_{CC})^{-1}$, $\tau' = (4\,^1J_{CC})^{-1}$, $\phi_1 = x, -x, x, -x$; $\phi_2 = x, x, -x, -x$; rec = $x, -x, -x, x$. (d) Soft HCCC-COSY to determine the $^3J_{C'C\gamma}$ coupling constants. $\Delta = (2\,^1J_{CH})^{-1}$, $\Delta' = 18/(90\,^1J_{CH})$, $\tau = (2\,^1J_{CC})^{-1}$, $\tau' = 54/(90\,^1J_{CC})$, $\tau'' = \Delta' + t_2(0) + \tau_p(180°\,^{15}N)$, $\phi_1 = x, -x$; rec = $x, -x$. (e) 2D-ω_2-Cα,C'-decoupled ω_1-^{13}C-filtered NOESY to determine the $^3J_{H\alpha C\gamma}$ coupling constants. $\Delta = (2\,^1J_{CH})^{-1}$, $\phi_1 = x, -x, x, -x, x, -x, x, -x$; $\phi_2 = x, x, -x, -x$; $\phi_3 = x, x, x, x, -x, -x, -x, -x$; rec = $x, -x, -x, x, -x, x, x, -x$.

mixing pulse with $\beta = 36°$. The decoupling scheme was an expanded amplitude-modulated G3 pulse $G3^{ampl}(t) = G3 + \cos(\Delta\Omega t)G3(t)$ according to AA(A)BB(A)BA(B)AB(B) (MLEV-8/4) (Eggenberger et al., 1992b). The abbreviation AB(B) stands for the following: an on-resonance $G3_x$ = A is followed by an on-resonance $G3_{-x}$ = B pulse. During the interval of the pulses A and B, the amplitude-modulated off-resonance pulse in parentheses (B) = $\cos(\Delta\Omega t)G3(t)$ is applied with phase $-x$. On- and off-resonance pulses are simultaneously applied; therefore, the off-resonance G3 pulse is twice as long as the on-resonance G3 pulse. The MLEV-8 expansion for the on-resonance decoupling consists of AABB BAAB, and the MLEV-4-expansion for the off-resonance decoupling consists of AABB. Four shapes, AA(A), AB(A), BA(A), and BB(A), are sufficient to program the decoupling sequence on the Bruker AMX system. The data were processed in the same way as the SOFT-HCCH-COSY spectrum, except for the fact that no mirror image linear prediction was used in t_2.

The SOFT-HCCC-COSY sequence (Schwalbe et al., *J. Am. Chem. Soc.*, in press) used for the measurement of $^3J_{C'C\gamma}$ coupling constants is shown in Figure 2d. The fixed delays were $\Delta = 3.4$ ms, $\tau = 7.1428$ ms, $\tau' = 8.5714$ ms, $\tau'' = 1.4238$ ms, $\Delta' = 1.3794$ ms. The parameters had to be adjusted to yield spectra without phase correction in ω_1 and ω_2, since an evolution of chemical shift during the rather long aliphatic carbon-selective pulses cannot be neglected. Homospoil pulses of 2- and 1.5-ms duration and purge pulses of 2-ms duration were applied. Carbon pulses are selective for the aliphatic region of the ^{13}C spectrum (G4 and time-reversed G4 for alternating 90° pulses, G3 for 180° pulses). Two scans per t_1 (64 complex points, 4483 Hz) and t_2 (128 complex points, 1000 Hz) were recorded with 512 complex points in t_3. RSH in t_1 and States-TPPI (Bax et al., 1991) in t_2 were used for

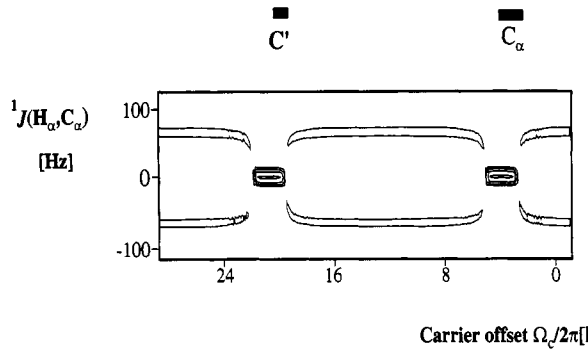

FIGURE 3: Double phase modulated decoupling of Cα and C′ resonances. Experimental decoupling efficiency demonstrated for the Hα-resonance of ^{13}C-labeled alanine in D_2O. The plot was obtained by decreasing the carbon frequency in steps of 100 Hz from 43 ppm (the center of the aliphatic carbon resonances). The band width of the decoupling region is 2.5 kHz, covering the Cα and C′ resonances as indicated. The phase shifts were 19750 and 2822 Hz downfield of the carrier frequency located in the middle of the aliphatic carbon resonances.

phase-sensitive detection. After FT in ω_2 and a strip transformation in ω_3, ranging from 1.23 to –0.25 ppm, mirror image linear prediction in ω_1 from 127 reflected complex points to 256 points was used. A cosine-squared apodization was then used for apodization. The final matrix comprised 256 × 512 × 256 real points ω_3, ω_2, and ω_1, respectively. The total measuring time was 27 h.

The experiment carried out to measure $^3J_{H\alpha C\gamma}$ couplings was a ω_1-^{13}C-filtered NOESY. It employs C_α and C′ doubly selective decoupling during acquisition to reduce the multiplicity on the $H_\gamma H_\alpha$ cross peak of interest. The pulse sequence is shown in Figure 2e. Carbon pulses are selective for the aliphatic region of the carbon resonances, applying Gaussian pulse cascades as described for the SOFT-HCCH-COSY experiment above. To achieve a C_α,C′-selective decoupling, a MLEV-16 expansion of doubly phase modulated G3 pulses with a duration of 2.2122 ms was used, yielding a decoupling performance shown in Figure 3. The phase shifts were 19 750 and 2822 Hz downfield of the carrier frequency located in the middle of the aliphatic carbon resonances. The decoupled band width was 2.2 kHz, covering the C_α-resonances of the eight valine residues (67.7–59.0 ppm). States-TPPI was used for frequency sign discrimination in ω_1. The mixing time τ_m was 200 ms. A 3-ms homospoil pulse was applied in the middle of the mixing period. The spectral width covered 5 kHz in both dimensions. A total of 56 scans with 3072 data points (t_2) were collected for each of the 1024 t_1 increments. The data were processed with squared cosine apodization functions in both dimensions and zero-filled to yield 4096 × 1024 real spectrum points after FT. The total measurement time was 28 h.

RESULTS

The conformational analysis of the valine side chains in RNase T_1 requires the quantitative determination of ^3J coupling constants relevant to the χ_1 angle. The coupling constant information then has to be translated into dihedral angles. Finally, the obtained geometries were examined for consistency with the coupling constants associated with C_γ and with NOE information.

Evaluation of ^3J Coupling Constants. The relative shift between the 1D spectral traces obtained from the upper and lower half of an E.COSY multiplet yields the desired coupling constant (Griesinger et al., 1985, 1987). The drawback of manual alignment procedures is the subjective criterion for the "best fit" of the two traces. To determine accurate $^3J_{H\alpha H\beta}$, $^3J_{C'H\beta}$, and $^3J_{NH\beta}$ coupling constants without bias, we have used a semiautomatic trace-fitting procedure for the quantitative analysis of E.COSY multiplets (Schmidt, J. M. & Ernst, R. R., unpublished). The proposed method is based on a continuous rather than on a point-by-point alignment, such that the accuracy of the determined coupling constant becomes independent of the digital resolution.

In essence, the evaluation procedure involves the convolution of one of the two traces with a frequency-shifting function $\delta(2\pi J)$, where J represents the desired coupling constant which has to be iteratively adjusted. For each E.COSY multiplet, two ω_3 traces, denoted $S^u(\omega_3)$ and $S^l(\omega_3)$ corresponding to the upfield and lowfield half of the multiplet, were obtained by summing over the spectral points in ω_1 and ω_2. Complex ω_3 data were retained for both spectrum traces. For the determination of $^3J_{NH\beta}$, the traces consisted of 64 data points (= 113.2 Hz), while in the case of $^3J_{H\alpha H\beta}$ and $^3J_{C'H\beta}$, the traces comprised 32 data points (= 108.5 Hz). In practice, convolution was performed in three steps, inverse Fourier transformation of the lower trace, multiplication with a complex exponential factor $\exp(i2\pi Jt)$ and Fourier transformation of the product, as given by

$$S^l(\omega_3 + 2\pi J) = A \cdot \mathrm{FT}\{S^l(t_3)\exp(i2\pi J t_3)\} \quad (1)$$

The scaling factor A accounts for different signal amplitudes. The parameters A and J were optimized in a nonlinear fit procedure using the SIMPLEX algorithm (Nelder & Mead, 1965) based on the least-squares criterion given by

$$\chi^2 = \sum_{k=1}^{n} \{S^u{}_k(\omega_3) - S^l{}_k(\omega_3 + 2\pi J)\}^2 \quad (2)$$

where k runs over the n spectral points. The J coupling constants obtained from the fit are summarized in Table 1. The variances in the ^3J values were obtained by error-propagation analysis and error calculation (Clifford, 1973), assuming that the spectral points were not correlated and that their intensities exhibit uniform variances equal to the mean squared-noise intensity (arbitrarily set to 1 in eq 2). The variances in the ^3J values were obtained by numerical differentiation of $S^l(\omega_3 + 2\pi J)$ with respect to the parameter J according to

$$\sigma_J{}^2 = \left(\frac{\partial J}{\partial S}\right)^2 \sigma_S{}^2 = \frac{\chi^2}{\upsilon}\sum_{k=1}^{n}\left\{\frac{S^l{}_k(\omega_3 + 2\pi(J+\epsilon)) - S^l{}_k(\omega_3 + 2\pi(J-\epsilon))}{2\epsilon}\right\}^{-2} \quad (3)$$

where ϵ was 0.01 Hz and υ represents the degrees of freedom in the fit, i.e., $(n-2)$ in this case. The fit quality was given by the R factor evaluated according to

$$R = \chi^2 / \sum_{k=1}^{n}\{S^u{}_k(\omega_3)\}^2 \quad (4)$$

The standard deviations of the J coupling constants and the R factors are listed in Table 1.

A quantitative determination of the $^3J_{H\alpha C\gamma}$ and $^3J_{C'C\gamma}$ coupling constants was carried out according to Schwalbe et al. (1993).

Evaluation of χ_1 Dihedral Angles. Valine side-chain dihedral angles were obtained by fitting one or multiple χ_1

Table 1: Experimental ^3J Coupling Constants of Valine Residues in RNase T_1

residue	$^3J_{H\alpha H\beta}$ (Hz)	R	$^3J_{C'H\beta}$ (Hz)	R	$^3J_{NH\beta}$ (Hz)	R	$^3J_{H\alpha C\gamma l}{}^{a,b}$ (Hz)	$^3J_{H\alpha C\gamma u}{}^{a,b}$ (Hz)	$^3J_{C'C\gamma l}{}^{a}$ (Hz)	$^3J_{C'C\gamma u}{}^{a}$ (Hz)
Val16	12.4 ± 0.86	0.11	0.5 ± 0.42	0.03	−1.7 ± 0.19	0.01	1.1 ± 0.8	1.3 ± 0.8	4.3 ± 0.12	1.1 ± 0.14
Val33	5.5 ± 0.70	0.05	2.1 ± 0.38	0.02	−2.1 ± 0.42	0.40	0.8 ± 0.8	3.8 ± 0.8	2.3 ± 0.12	1.2 ± 0.15
Val52	6.4 ± 0.56	0.04	0.9 ± 0.49	0.02	−4.2 ± 0.60	0.27	2.0 ± 0.8	4.8 ± 0.8	3.7 ± 0.11	1.4 ± 0.15
Val67	9.2 ± 0.42	0.02	1.0 ± 0.33	0.02	−2.6 ± 0.27	0.01	0.0 ± 0.8	2.0 ± 0.8	1.5 ± 0.46	3.8 ± 0.09
Val78	5.2 ± 0.50	0.03	2.6 ± 0.60	0.01	−3.8 ± 0.38	0.14	nd[c]	nd[c]	nd[c]	nd[c]
Val79	12.7 ± 0.74	0.10	0.9 ± 0.73	0.23	−2.5 ± 0.35	0.05	1.4 ± 0.8	1.8 ± 0.8	1.3 ± 0.31	4.5 ± 0.36
Val89	12.0 ± 0.8[b]	nd[b]	2.6 ± 0.38	0.04	−0.9 ± 0.37	0.06	1.3 ± 0.8	1.1 ± 0.8	4.8 ± 0.60	1.1 ± 0.07
Val101	3.6 ± 0.47	0.05	0.7 ± 0.35	0.04	−4.6 ± 0.40	0.40	2.6 ± 0.8	4.2 ± 0.8	3.0 ± 0.05	0.6 ± 0.16

[a] The indices l and u refer to the *low*-field and *high*-field carbon resonances, respectively, as given in Table 3. [b] A global error of ±0.8 Hz (1 datapoint) was assumed, since error determination was not possible due to spectral overlap. [c] nd, not determined as the chemical shifts of both Hγ and Cγ resonance pairs are degenerate at the experimental conditions.

rotamers to the set of experimental coupling constants $^3J_{H\alpha H\beta}$, $^3J_{C'H\beta}$, and $^3J_{NH\beta}$. The analysis is based on the assumptions that the geometry at the two carbon sites C_α and C_β is perfectly tetrahedral. Substituent effects on the J coupling constants were disregarded. The dihedral angle dependence of the ^3J coupling constants (in hertz) used for the fit is then given by

$$^3J_{H\alpha H\beta} = 9.5\cos^2(\chi_1) - 1.6\cos(\chi_1) + 1.8$$

(DeMarco et al., 1978a) (5a)

$$^3J_{C'H\beta} = 7.20\cos^2(\chi_1 + 120°) - 2.04\cos(\chi_1 + 120°) + 0.6$$

(Fischman et al., 1980) (5b)

$$^3J_{NH\beta} = -4.4\cos^2(\chi_1 - 120°) + 1.2\cos(\chi_1 - 120°) + 0.1$$

(DeMarco et al., 1978b) (5c)

The Karplus parameters for the calculation of $^3J_{NH\beta}$ coupling constants have been determined with different model compounds. DeMarco and co-workers derived these $^3J_{NH\beta}$ coefficients from the peptide alumichrome in solution, utilizing the crystallographic torsion angles determined for the peptide analog ferrichrome. Coefficients for the dihedral angle dependence of $^3J_{C'H\beta}$ were determined from a constrained bicyclooctane derivative (Fischman et al., 1980). For the same compound, also $^3J_{NH\beta}$ coefficients were obtained according to

$$^3J_{NH\beta} = -3.75\cos^2(\chi^1 - 120°) + 0.26\cos(\chi_1 - 120°) - 0.54$$

(Fischman et al., 1980) (5d)

In order to get some insight into the effect of variations in the Karplus parameters on the conformational analysis, both sets (eqs 5a–c and eqs 5a,b,d) were used for the dihedral angle determination. Figure 4 shows the two so-called Karplus relations obtained from the two different sets of $^3J_{NH\beta}$ coefficients.

Since no reliable parametrizations for the $^3J_{C'C\gamma}$ and $^3J_{H\alpha C\gamma}$ coupling constants are known from the literature, these coupling constants were not considered in the quantitative evaluation of valine χ_1 angles; rather, they were used for the stereospecific assignment of the methyl resonances.

In general, an amino acid side chain is not necessarily restricted to a single conformation. Internal motion may lead to an averaging of the observed ^3J coupling constants. Therefore, three different models of internal dynamics (denoted A, B, and C) were applied to describe the most probable χ_1 angle or the χ_1 angle distribution. In model A, a fixed χ_1 value was assumed in a single-parameter fit to minimize the difference between the calculated and experimental coupling constants according to

$$J_i^{exp} \equiv J_i^{calc}(\chi_1) \quad (6)$$

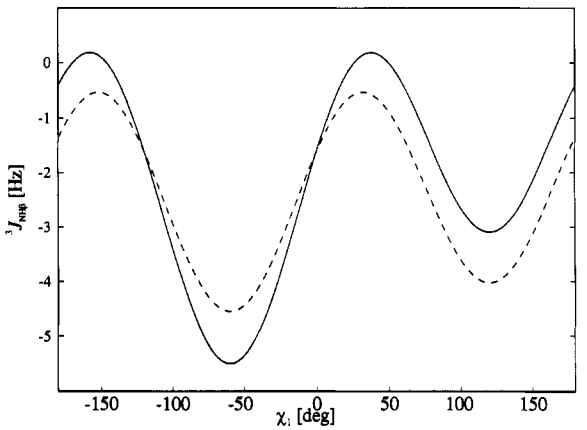

FIGURE 4: The dihedral angle dependence of $^3J_{NH\beta}$. The solid line represents data derived from studies of alumichrome by DeMarco and co-workers (1978b); the dashed line represents the data obtained from a bicyclooctane derivative (Fischman et al., 1980).

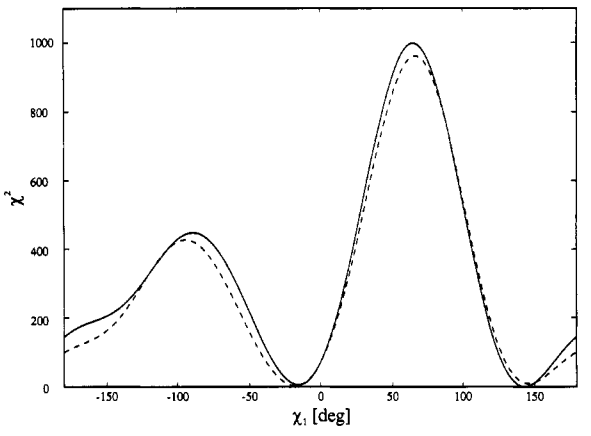

FIGURE 5: Error profiles χ^2 versus dihedral angle χ_1 calculated for Val67. Model A (eq 6) was used with the two different sets of Karplus parameters given in eqs 5a–c (solid lines) and in eqs 5a,b,d (dashed lines), respectively.

where i indicates the pair of the coupling nuclei according to eq 5. In model B, the dihedral angle was allowed to exhibit local mobility according to a unimodal Gaussian distribution, leading to a two-parameter fit of $\langle\chi_1\rangle$ and σ_{χ_1} as given by

$$J_i^{exp} \equiv J_i^{calc}(\langle\chi_1\rangle, \sigma_{\chi_1}) = \int_{-\pi}^{+\pi} p(\chi_1) J_i^{calc}(\chi_1)\, d\chi_1 = \frac{1}{\sigma_{\chi_1}\sqrt{2\pi}} \int_{-\pi}^{+\pi} J_i^{calc}(\chi_1) \exp\left\{-\frac{(\chi_1 - \langle\chi_1\rangle)^2}{2\sigma_{\chi_1}^2}\right\} d\chi_1 \quad (7)$$

In a three-site jump model (model C) comprising the three staggered rotamers with $\chi_1 = 180°$, −60°, and +60°, the respective populations p_I, p_{II}, and p_{III} were allowed to vary, leading again to a two-parameter fit of p_I and p_{II} according

Table 2: Side-Chain Geometries of Valine Residues in RNase T_1 As Derived from ^3J Coupling Constants According to Different Models

	χ^1 (deg)	$\langle\chi^1\rangle \pm \sigma_{\chi^1}$ (deg)	p_I (%)	p_{II} (%)	p_{III} (%)	$^3J_{H\alpha H\beta}$ (Hz)	$^3J_{CH\beta}$ (Hz)	$^3J_{NH\beta}$ (Hz)	χ^2	Q (%)	χ^1 (deg)	$\langle\chi^1\rangle \pm \sigma_{\chi^1}$ (deg)	p_I (%)	p_{II} (%)	p_{III} (%)	$^3J_{H\alpha H\beta}$ (Hz)	$^3J_{CH\beta}$ (Hz)	$^3J_{NH\beta}$ (Hz)	χ^2	Q (%)
										Val16										
A	159					11.57	0.46	−1.62	1.15	**56**	172					12.72	0.87	−1.78	0.91	**63**
B		159 ± (<1)				11.56	0.46	−1.63	1.16	28		172 ± (<1)				12.71	0.86	−1.79	0.92	34
C			77	23	0	10.74	1.38	−1.56	8.47	0			91	9	0	12.00	1.38	−1.65	4.41	4
										Val33										
A	129					6.57	2.26	−3.01	7.91	**2**	−34					6.53	2.28	−3.95	22.87	0
B		129 ± 11				6.56	2.45	−2.89	7.56	1		−34 ± 36				6.28	2.45	−3.14	9.00	0
C			36	51	13	6.81	2.51	−2.98	9.97	0			32	56	12	6.45	2.39	−3.13	9.33	0
										Val52										
A	−37					6.61	0.46	−4.72	1.51	47	−39					6.32	0.46	−4.04	0.83	**66**
B		−37 ± 16				6.46	0.96	−4.47	0.20	**65**		−39 ± 12				6.29	0.76	−3.91	0.38	54
C			26	74	0	6.24	1.38	−3.97	1.35	24			30	70	0	6.19	1.38	−3.60	2.32	13
										Val67										
A	143					9.17	0.94	−2.51	0.12	**94**	−18					8.92	1.38	−2.77	2.54	**28**
B		143 ± (<1)				9.16	0.95	−2.52	0.12	73		−18 ± (<1)				8.89	1.36	−2.79	2.55	11
C			60	40	0	9.06	1.38	−2.46	2.05	15			61	39	0	9.21	1.38	−2.59	1.62	20
										Val78										
A	123					5.44	3.05	−3.09	4.14	13	123					5.47	3.02	−4.02	1.27	**53**
B		−55 ± 41				5.22	2.68	−3.83	0.05	82		−53 ± 34				5.07	2.28	−3.54	0.69	41
C			19	66	15	5.20	2.60	−3.79	0.00	**97**			18	70	12	5.08	2.40	−3.59	0.39	**53**
										Val79										
A	156					11.24	0.46	−1.78	8.04	**2**	164					12.16	0.54	−2.26	1.11	**57**
B		156 ± (<1)				11.24	0.46	−1.79	8.05	0		164 ± (<1)				12.15	0.54	−2.27	1.11	29
C			75	25	0	10.51	1.38	−1.68	14.16	0			85	15	0	11.44	1.38	−1.84	6.54	1
										Val89										
A	−168					12.48	2.43	0.04	7.21	3	−166					12.31	2.64	−0.76	0.32	85
B		−173 ± 24				11.24	2.40	−0.59	1.98	16		−167 ± 18				12.00	2.61	−0.91	0.00	**100**
C			83	4	13	11.29	2.43	−0.63	1.59	**21**			86	0	14	11.59	2.54	−1.35	1.69	19
										Val101										
A	−55					4.02	1.02	−5.45	6.16	**5**	−56					3.93	1.06	−4.53	1.84	**40**
B		−55 ● 6				4.04	1.08	−5.41	6.12	1		−56 ± (<1)				3.91	1.07	−4.53	1.86	17
C			7	93	0	4.00	1.38	−5.17	6.63	1			1	99	0	3.51	1.38	−4.50	4.12	4

[a] The geometries given on the left half of the table were obtained from the first set of Karplus coefficients according to eqs 5a–c, whereas the results on the right were obtained with the second set (eqs 5a,b,d). A, B, and C denote different models for conformational flexibility as explained in the text. Underlined values for calculated ^3J coupling constants deviate from experiment by more than σ_J given in Table 1. Q values given in bold letters indicate the best fitting model for each residue.

to

$$J_i^{exp} \equiv J_i^{calc}(p_I, p_{II}) = p_I J_i^{calc}(\chi_1 = 180°) + p_{II} J_i^{calc}(\chi_1 = -60°) + p_{III} J_i^{calc}(\chi_1 = +60°) \quad (8)$$

$$p_{III} = 1 - p_I - p_{II}$$

More complicated models, e.g., multimodal Gaussian distributions, could not be applied, since the number of geometry variables would exceed the number of experimental J coupling constants.

Least-squares optimization of the parameters χ_1, or $\langle\chi_1\rangle$ and σ_{χ_1}, or p_I and p_{II}, in the models A, B, and C, respectively, was achieved again using the SIMPLEX algorithm (Nelder & Mead, 1965) for minimizing the error function

$$\chi^2 = \sum_{i=1}^{3} \left(\frac{(J_i^{exp} - J_i^{calc})}{\sigma_{J_i}} \right)^2 \quad (9)$$

where σ_J are the standard deviations of the experimental ^3J coupling constants as given in Table 1. The calculated average coupling constants and the geometry parameters obtained with the two sets of Karplus parameters for the eight valine side chains are listed in Table 2. The significance of the results of the different models was evaluated using the χ^2 probability function $Q(\chi^2,\upsilon)$ according to Press et al. (1989)

$$Q(\chi^2,\upsilon) = \Gamma\left(\frac{\chi^2}{2}, \frac{\upsilon}{2}\right) / \Gamma\left(\frac{\upsilon}{2}\right) \quad (10)$$

assuming that the distribution of the experimental errors σ_J is given by a Gaussian distribution function. Note that υ, the number of degrees of freedom, varies for the different models. The fit errors χ^2 and the significance parameters Q are also given in Table 2.

Valine Side-Chain Conformations in Ribonuclease T_1. The two parts of Table 2 correspond to the two different sets of Karplus parameters used for the calculation of ^3J coupling constants. In almost all cases, the optimized conformations are very similar for both sets. Only in the case of Val67, the optimal χ_1 angles derived with models A and B differ considerably. This may indicate two geometric solutions, as will be discussed below.

The wide range of Q values obtained in the determination of χ_1 angles renders it somewhat difficult to accept or reject a fit result; a threshold of 10% seems reasonable. It is evident that for Val16, Val52, and Val78 simple models for the side-chain geometries can be found with either set of Karplus parameters that agree with the experimental coupling constants on a more than 50% significance level. In the case of Val67 and Val89, the Q values also indicate an acceptable fit. However, for these residues, the probability of the optimized conformations depends strongly on the Karplus parameters used. For Val79 and Val101, the fit quality is very sensitive to the variation in the Karplus parameters, as indicated by the improvement of the fit with the second set. For Val33, the Q values are rather small, indicating a severe inconsistency between the experimental data and the conformational model. Indeed none of the conformations fits the measured coupling

constants within experimental errors. In the following, the results of the dihedral angle fit for each valine side chain are discussed in more detail.

For Val16, the results indicate that the predominant rotameric state is slightly distorted from the staggered conformation with $\chi_1 = 180°$. The exact χ_1 value varies depending on the set of Karplus equations ($\chi_1 = 159°$ (set 1) and $\chi_1 = 172°$ (set 2)). The ideal staggered geometry would lead to a noticeable decrease in the significance as indicated for model C. A single rigid conformation (model A) fits experimental data best.

Val33 occupies all three staggered states according to model C, although with a low Q value. The preferred χ_1 angle derived from model A, which gives the best fit to the experiment, differs from the main rotamer derived from the staggered-rotamer model (model C). Nevertheless, the latter conformational equilibrium is in better agreement with NOE data as will be discussed below. In conclusion, the preferred rotamer is likely to exhibit a χ_1 value of $-60°$.

For Val52, a Gaussian distribution with a width of $\pm 16°$ about a mean χ_1 of $-37°$ yielded a very good fit ($Q = 65\%$) to the experimental ^3J coupling constants, when Karplus coefficients of set 1 are used. According to the set 2 of Karplus parameters, the significance for model A, which neglects local mobility, is slightly larger (66%). However, the mean χ_1 angle is nearly identical with both sets ($\chi_1 = -37°$ and $-39°$, respectively).

In the case of Val67, a single rigid conformation with $\chi_1 = 143°$ is in almost perfect agreement with the experiment ($Q = 94\%$), if the first set of Karplus parameters is used. From set 2, $\chi_1 = -18°$ with a markedly lower significance. The χ^2 error profiles obtained with model A show (Figure 4) that two geometric arrangements are possible for this side chain, irrespective of the applied set of Karplus parameters. However, the NOE data better agree with a χ_1 angle near 180°, as will be discussed later.

Using the Karplus parameter set 1 for the Val78 side chain, a conformational equilibrium between the three staggered rotamers emerges with a 97% probability. However, a broad Gaussian χ_1 distribution with a large width of $\pm 41°$ about $-55°$ also matches the data, with a slightly lower probability of 82%. The main rotamer is in any case that with a χ_1 angle close to $-60°$. Similar results were obtained with the parameter set 2, although in this case, models A and C fit equally well ($Q = 53\%$). It should be noted that the single rigid conformation (model A) exhibits a χ_1 angle of 123°, indicating again the possibility of two geometric solutions.

The side chain of Val79 is best described assuming a rigid conformation with a χ_1 angle close to 180°. The fit improved drastically with the second set of Karplus parameters, while the optimal conformation does not change significantly.

The conformations obtained for the Val89 side chain are very similar with both parameter sets. However, the fits are very sensitive to a variation in the $^3J_{NH\beta}$ Karplus coefficients. According to set 2, a Gaussian distribution about a χ_1 angle of $-167°$ gives a perfect fit to experiment, while set 1 delivers a three-state equilibrium with the main rotamer $\chi_1 = 180°$ ($Q = 21\%$).

For Val101, a single side-chain conformation with $\chi_1 = -56°$ explained experimental data best, which is in agreement with the preferred rotameric state, $\chi_1 = -60°$, obtained from model C. As for Val79, a remarkable sensitivity of the fit with respect to different sets of Karplus parameters was found.

Quantification of the $^3J_{H\alpha C\gamma}$ Coupling Constants. The angular dependence of vicinal proton–carbon coupling constants is known from theoretical calculations (Wasylishen & Schaefer, 1972) as well as from experimental data (DeMarco & Llinás, 1979). Wasylishen and Schaefer described theoretical J_{trans} and J_{gauche} values of 8.82 and 1.98 Hz for hydrocarbons, while DeMarco and Llinás determined J_{trans} and J_{gauche} values of 11.7 and 2.02 Hz for the $^3J_{C\alpha H\gamma}$ coupling constants of the ornithine residues of alumichrome. These values are significantly larger than the $^3J_{H\alpha C\gamma}$ values observed for the valine side chains in RNase T_1. In particular, the predicted J_{trans} coupling constant is not consistent with our findings. For the presumable Val101 conformation with $\chi_1 \approx -60°$, as derived from the three other coupling constants, a nearly perfect trans geometry has to be assumed for $H\alpha$–$C\gamma_1$. However, the corresponding value of $^3J_{H\alpha C\gamma_1}$ is smaller than expected.

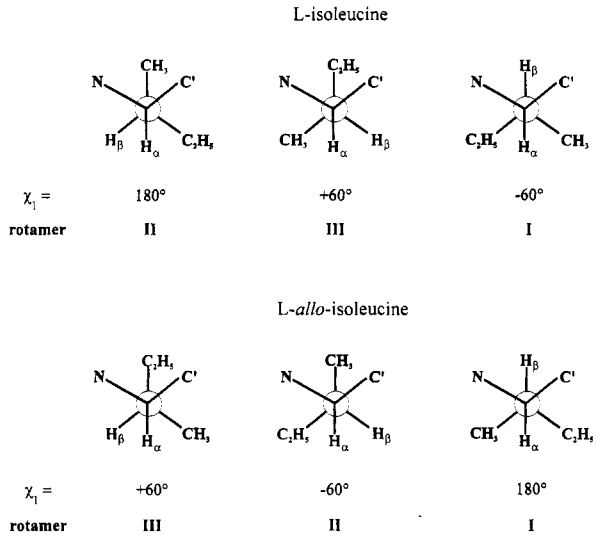

FIGURE 6: Designation of nuclei and χ_1 dihedral angle conformations in L-isoleucine and L-*allo*-isoleucine. Newman projections of the three staggered side chain rotamers together with the associated dihedral angle values are shown. According to the IUPAC nomenclature, $C_{\gamma 1}$ and $C_{\gamma 2}$ denote ethyl and methyl carbon positions, giving rise to a different substituent priority at C_β for isoleucine compared to valine.

To verify the $^3J_{H\alpha C\gamma}$ coupling constants found for the valine residues of RNase T_1, an attempt was made to determine J_{trans} and J_{gauche} values for $^3J_{H\alpha C\gamma}$ from the model compounds isoleucine and *allo*-isoleucine. The staggered χ_1 rotamers of these amino acids are shown in Figure 6; the IUPAC designation of the γ carbon atoms is given in the figure legend. $^3J_{H\alpha C\gamma 1}$ of *allo*-isoleucine and $^3J_{H\alpha C\gamma 2}$ of both compounds were determined by X-filtered TOCSY (Sattler et al., 1992) and refocused HMBC (Schwalbe et al., unpublished) experiments. In addition, $^3J_{H\alpha H\beta}$ coupling constants of both isoleucine and *allo*-isoleucine were measured. These coupling constants have been evaluated to characterize the side-chain conformations of the two amino acids and to derive J_{trans} and J_{gauche} values for $^3J_{H\alpha C\gamma}$ from the obtained conformations. The values measured for *allo*-isoleucine are 3.2 ± 0.1 Hz for $^3J_{H\alpha H\beta}$, 3.6 Hz for $^3J_{H\alpha C\gamma 1}$, and 5.3 Hz for $^3J_{H\alpha C\gamma 2}$. Assuming that the conformation of the *allo*-isoleucine side chain can be described in terms of staggered rotamers, the $^3J_{H\alpha H\beta}$ coupling constant indicates either a single gauche conformation or an equilibrium between the two gauche conformations with respect to the $H\alpha$ and $H\beta$ positions, i.e., either rotamer II or rotamer III or an equilibrium between these two states. Therefore, the $^3J_{H\alpha C\gamma}$ coupling constants determined for *allo*-isoleucine are conformationally averaged according to

$$p_{III}J_{H\alpha C\gamma 1,trans} + (1 - p_{III})J_{H\alpha C\gamma 1,gauche} = 3.6 \text{ Hz} \quad (11)$$

$$p_{III}J_{H\alpha C\gamma 2,gauche} + (1 - p_{III})J_{H\alpha C\gamma 2,trans} = 5.3 \text{ Hz} \quad (12)$$

Assuming that the angular dependencies of the two $^3J_{H\alpha C\gamma}$ coupling constants are identical, i.e., $J_{H\alpha C\gamma 1,trans} = J_{H\alpha C\gamma 2,trans}$ and $J_{H\alpha C\gamma 1,gauche} = J_{H\alpha C\gamma 2,gauche}$, the sum of J_{trans} and J_{gauche} is obtained from eqs 11 and 12 according to

$$J_{H\alpha C\gamma,trans} + J_{H\alpha C\gamma,gauche} = 8.9 \text{ Hz} \quad (13)$$

For isoleucine, a $^3J_{H\alpha H\beta}$ coupling constant of 3.9 ● 0.1 Hz was found. The $^3J_{H\alpha C\gamma 2}$ coupling constant in this amino acid is 3.0 Hz. The value of $^3J_{H\alpha C\gamma 1}$ in isoleucine could not be determined due to the lack of resolution. On the basis of the assumptions mentioned before, the side chain of isoleucine is therefore described by one of the rotameric states II or III (as indicated by $^3J_{H\alpha H\beta}$) or by a conformational equilibrium between these two rotamers. Thus, $^3J_{H\alpha C\gamma 2}$ in isoleucine is motionally averaged according to

$$(1 - p_{III})J_{H\alpha C\gamma 2,trans} + p_{III}J_{H\alpha C\gamma 2,gauche} = 3.0 \text{ Hz} \quad (14)$$

Assuming that the conformational equilibrium is identical for both epimeric compounds (which is not exactly true, since the $^3J_{H\alpha H\beta}$ coupling constants for the two epimers are slightly different), the value of 5.3 Hz determined for $^3J_{H\alpha C\gamma 2}$ in *allo*-isoleucine is used for $^3J_{H\alpha C\gamma 1}$ in isoleucine:

$$p_{III}J_{H\alpha C\gamma 1,trans} + (1 - p_{III})J_{H\alpha C\gamma 1,gauche} = 5.3 \text{ Hz} \quad (15)$$

From eqs 14 and 15, a value for the sum of J_{trans} and J_{gauche} is obtained:

$$J_{H\alpha C\gamma,trans} + J_{H\alpha C\gamma,gauche} = 8.3 \text{ Hz} \quad (16)$$

To summarize: Using either of the two data sets leads to a value of 8.6 ± 0.3 Hz for the sum of $^3J_{H\alpha C\gamma trans}$ and $^3J_{H\alpha C\gamma gauche}$.

With a $J_{H\alpha C\gamma,gauche}$ of 1.3 Hz found in many valine residues in ribonuclease T_1, a $^3J_{H\alpha C\gamma,trans}$ value of 7.6 Hz results according to eq 13 and of 7.0 Hz according to eq 16. A conformational equilibrium in *allo*-isoleucine and isoleucine between all three staggered rotamers rather than the two mentioned conformations would further decrease the value of $^3J_{H\alpha C\gamma,trans}$. Nevertheless, there is still a discrepancy between the $^3J_{H\alpha C\gamma,trans}$ coupling constants found in RNase T_1 and the values derived from both isoleucine and *allo*-isoleucine. Therefore, $^3J_{H\alpha C\gamma}$ coupling constants were used only qualitatively for stereospecific assignments rather than for the quantitative evaluation of side-chain conformations.

Stereospecific Assignment of Valine Methyl Resonances. The stereospecific valine methyl resonance assignments were achieved from qualitatively evaluating the relative magnitudes of the pairwise $^3J_{C'C\gamma}$ and $^3J_{H\alpha C\gamma}$ coupling constants. Since these vicinal coupling constants are also associated with the χ_1 angle in valine side chains, the side-chain conformational equilibria derived from the set of ^3J data involving H_β have to be consistent with these coupling constants.

Similar magnitudes for both $^3J_{C'C\gamma}$ couplings together with different values for the two $^3J_{H\alpha C\gamma}$ coupling constants (values differing by more than 1 Hz are considered "different") are indicative for a predominant side-chain conformation with $\chi_1 \approx +60°$ (Figure 1). For this rotamer, the larger $^3J_{H\alpha C\gamma}$ coupling constant is associated with the $C_{\gamma 1}$ position. Conversely, different $^3J_{C'C\gamma}$ and similar $^3J_{H\alpha C\gamma}$ coupling constants hint at a $\chi_1 \approx 180°$ conformation, for which the larger $^3J_{C'C\gamma}$ coupling constant is related to the $C_{\gamma 2}$ position. Finally, different magnitudes for either pair of couplings, $^3J_{H\alpha C\gamma}$ and $^3J_{C'C\gamma}$, are evidence for a $\chi_1 \approx -60°$ conformation of the side chain. Here, the larger $^3J_{H\alpha C\gamma}$ and the larger $^3J_{C'C\gamma}$ coupling constants are connected with the $C_{\gamma 2}$ and $C_{\gamma 1}$ positions, respectively. Hence, the $C_{\gamma 1}$ and $C_{\gamma 2}$ positions are identified with a high degree of certainty.

Table 3: Stereospecific Resonance Assignments (in ppm) of Valine Methyl Groups in RNase T_1[a]

	pro-R		*pro-S*	
residue	$\delta(^{13}C\gamma_1)$	$\delta(^1H\gamma_1)$	$\delta(^{13}C\gamma_2)$	$\delta(^1H\gamma_2)$
Val16	23.1	0.73	24.4	0.68
Val33	23.5	1.03	21.6	1.12
Val52	22.9	0.86	19.4	0.69
Val67	23.4	1.20	23.1	1.02
Val78	23.7	1.00	23.7	1.00
Val79	23.7	0.34	21.4	0.00
Val89	21.8	0.68	22.9	0.01
Val101	23.3	1.03	20.4	0.89

[a] Chemical shifts refer to 1-(trimethylsilyl)propionate-*2,2,3,3-d*$_4$ (TSP). ^1H and ^{13}C shifts at 308 K are taken from Weisemann and Rüterjans (unpublished).

Table 4: Qualitative Intraresidual NOE Intensities of Valine Residues in RNase T_1[a]

residue	$\sigma(\alpha\beta)$	$\sigma(\alpha\gamma_1)$	$\sigma(\alpha\gamma_2)$	$\sigma(N\beta)$	$\sigma(N\gamma_1)$	$\sigma(N\gamma_2)$
Val16	weak	strong	strong	medium	medium	strong
Val33	strong	strong	medium	weak	weak	strong
Val52	medium	medium	medium	weak	strong	strong
Val67	weak	medium	medium	strong	medium	strong
Val78	weak	nr[b]	nr[b]	weak	nr[b]	nr[b]
Val79	absent	strong	strong	weak	absent	strong
Val89	nd[c]	nd[c]	nd[c]	medium	medium	strong
Val101	strong	strong	strong	weak	medium	strong

[a] As given by Hoffmann and Rüterjans (1988). [b] nr, not resolved due to degenerate Hγ shifts. [c] nd, not detected due to presaturation of the Hα resonance.

According to the given qualitative classification, the predominant side-chain rotamer adopts a χ_1 angle of 180° in Val16, Val67, Val79, and Val89, while $\chi_1 \approx -60°$ in Val33, Val52, and Val101. No coupling constants could be obtained for Val78 due to degenerate resonances. The stereospecific assignments derived from J coupling information involving C_γ nuclei are summarized in Table 3. It should be emphasized that so far no NOE information was used in the analysis.

Comparison of the Obtained Side-Chain Conformations with NOE Data. The side-chain conformations derived from the analysis of ^3J coupling constants were also examined for consistency with qualitative intraresidue NOE intensities pertinent to the χ_1 angle in valine residues. As shown in Table 4, NOE intensities (Hoffmann & Rüterjans, 1988) were semiquantitatively classified into four categories ranging from absent to strong. In most cases, the preferred rotamer as obtained from the analysis of ^3J coupling constants is in good agreement with NOE data. Val16, Val67, Val79, and Val89 show relative Hα–Hγ and HN–Hγ NOE intensities that are characteristic of a χ_1 angle close to 180°, while for Val33, Val52, Val78, and Val101, the intensity patterns are qualitatively consistent with $\chi_1 \approx -60°$. In most cases, the NOE data are also in agreement with the stereospecific assignments of methyl resonances. Only for residues Val52 and Val101, an apparent inconsistency arises from the similar Hα–Hγ1 and Hα–Hγ2 NOE intensities, as the predominantly gauche oriented side chain ($\chi_1 \approx -60°$) should lead to a stronger NOE for Hα–Hγ$_1$ and to a smaller NOE for Hα–Hγ$_2$. However, this effect is attributed to the crude categorization

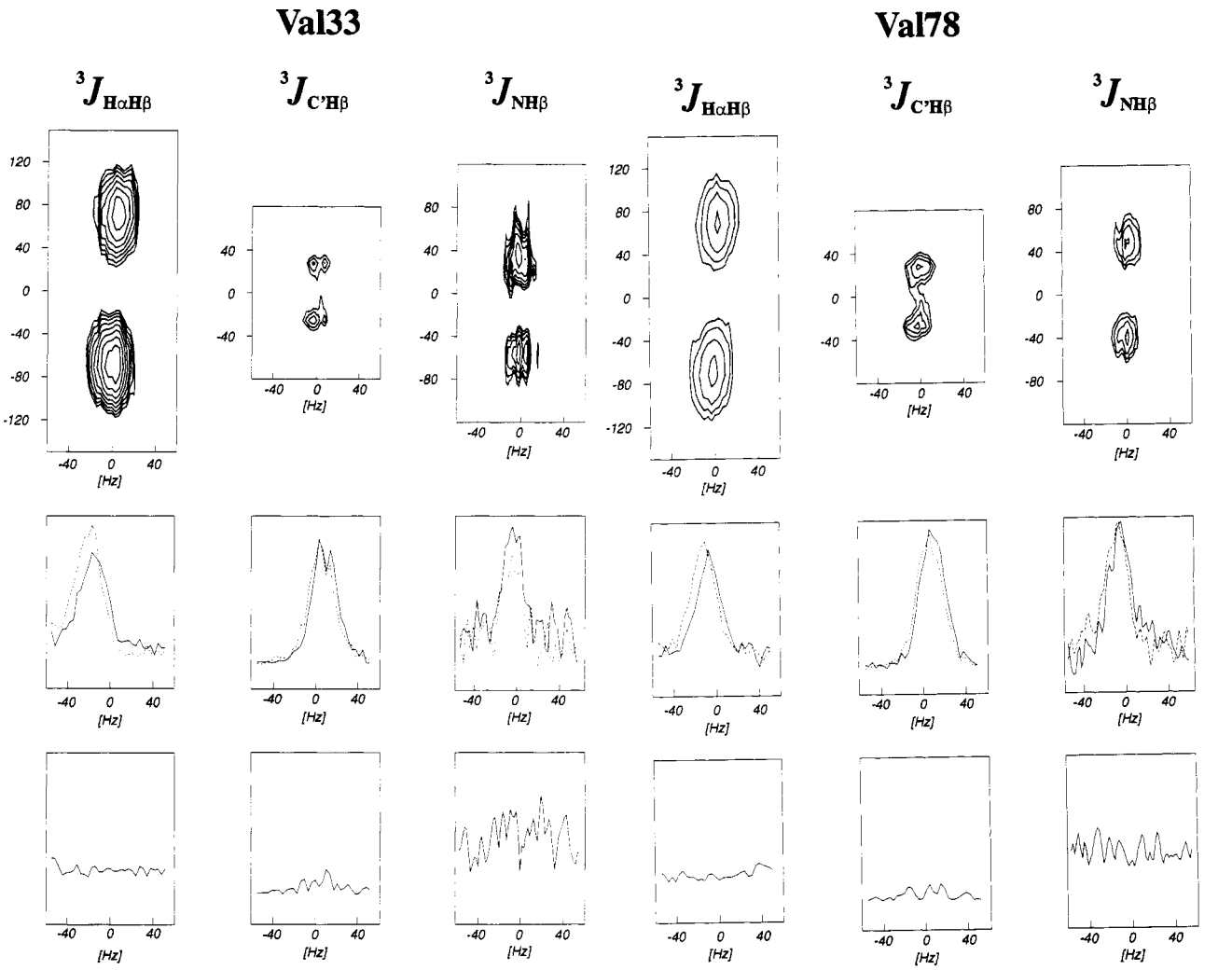

FIGURE 7: Experimental E.COSY multiplets of (left) Val33 and (right) Val78 recorded with the pulse sequences shown in Figure 3a–c. The depicted (ω_2, ω_3) multiplets are 2D ω_1 projections taken at the chemical-shift coordinates (Hα, Cα, Hβ), (Hα, Cα, Hβ), and (N, H^N, Hβ). For each multiplet, the relevant traces $S^u(\omega_3)$ (solid lines) and $S^l(\omega_3)$ (dashed lines) (as described in the text) are shown together with the difference spectrum obtained from the best superposition. Val78 and Val33, respectively, represent the best and worst fitting coupling topologies in the dihedral angle optimization.

and to the overlap present in the aliphatic region of the 2D NOESY spectrum.

DISCUSSION

The accuracy of the obtained side-chain conformations should be discussed in view of systematic errors which have not yet been considered. Systematic errors arise from the performance of the NMR experiments, from the assumptions made in the evaluation procedures and from simplifications in the conformational description. Due to the simplifying assumptions in the statistical analysis, it is likely that the calculated standard deviations underestimate the actual errors in some instances. As a consequence, the accuracy of the side-chain conformations obtained from the χ_1 angle fit might be higher than the Q values suggest.

Systematic Errors in the Experiments. A reasonable explanation for the discrepancies between calculated and experimental coupling constants are systematic errors in the experimental ^3J data which are not reflected by the standard deviations obtained from the statistical analysis. As pointed out recently by Norwood (1993) and Harbison (1993), this includes relaxation phenomena like differential relaxation, leading to apparently shifted resonance frequencies. Since this effect depends mainly on the relaxation behavior of the *passive* spin, we expect these errors to be small for all experiments except for the soft HCCH-E.COSY experiment, as this is the only pulse sequence using a proton as passive spin.

Furthermore, proton–proton couplings evolve in the refocussing period immediately prior to the acquisition period of the soft HCCH-E.COSY. The two E.COSY traces acquire a different phase modulation $\delta\varphi$ depending on the refocusing delay Δ and on the actual coupling $^3J_{H\alpha H\beta}$ according to

$$\delta\varphi = 360° \cdot {}^3J_{H\alpha H\beta} \cdot \Delta \qquad (17)$$

Another systematic error arises from the small-angle mixing pulse of 36° used in the soft HCCH-E.COSY in order to suppress the correlation of nonconnected transitions in the E.COSY cross peak.

For Val33, no appropriate fit of experimental ^3J values could be achieved, while for Val78, a very good fit of experimental coupling constants was obtained. Possibly, the differences in the linewidth and/or lineshapes between the two parts of the E.COSY cross peaks in all three spectra are more pronounced for Val33 than for Val78 (Figure 7).

Systematic Errors in the Evaluation Procedures. The translation of J coupling information into geometry parameters mainly suffers from the fact that a possibly very complex ensemble of conformations is characterized on the basis of

only a few J coupling constants. The single-site model A is the simplest description of the valine side-chain geometry. However, a rigid χ_1 angle gave satisfactory results in only four (Val16, Val79, Val67, and Val101) out of eight investigated residues.

For Val33, Val52, and Val89, unimodal χ_1 angle distributions (model B) according to a Gaussian function fit the experimental coupling constants better than the simple rigid-angle model. In case the optimal χ_1 value is identical with both models A and B, it was observed that the fit error χ^2 decreased systematically for a distribution in χ_1 compared to a rigid conformation. Here, the improvement of the fit is a consequence of allowing for χ_1 angle fluctuations within a torsional potential well, which is connected with an averaging of the calculated J coupling constants. In the limiting case, the width of the Gaussian curve collapses to zero, and identity between the two models is achieved, e.g., for Val16, Val67, and Val79. Still, the confidence Q is in favor of the simpler model as it requires only one adjustable parameter.

One might argue that the empirical Karplus parameters used in the calculation of coupling constants were calibrated with model compounds that also exhibit—to a limited extent—internal dynamics and that the coefficients are therefore expected to already account for averaging due to local angular oscillations. This would make the Gaussian model B obsolete. In fact, for moderate deviations (σ_{χ_1} = 5–10°), the effect of averaging on the calculated coupling constants is much smaller than the precision of the experimental coupling constants, i.e., below 0.1 Hz as exemplified by Val101 in Table 2. A larger scatter of χ_1 ($\sigma_{\chi_1} > 15°$) is required to produce significant effects.

In the staggered-rotamer analysis (model C), the torsion angles are constrained to specific values. This imposes severe limitations on the conformational characterization of a dihedral angle distribution. Although the assumption of staggered rotamers is reasonable from energetic considerations, X-ray results (Smith et al., 1986) indicate that even mobile side chains in proteins do occur in twisted conformations and are not necessarily constrained to staggered states. The Pachler-like analysis (model C) might therefore be insufficient to characterize amino acid side-chain geometries in proteins. The original Pachler analysis (Pachler, 1963, 1964) relies on two experimental coupling constants to solve a two-equation system, occasionally leading to negative populations for the third conformation p_{III} (Kessler et al., 1987). Constraining all populations to positive numbers, as was done in our analysis, clearly deteriorates the fit with model C in those cases for which one rotamer is not populated (Val16, Val52, Val67, Val79, and Val101). It is interesting to note that for the valine side chains which occupy all three rotameric states (Val78 and Val89), the Pachler model surpasses the Gaussian model in the characterization of the side-chain conformation.

Alternative models with more than two adjustable parameters require an extended set of observables, e.g., J coupling constants. With the limited set of coupling constants available, ambiguities will arise in the dihedral angle fit as a consequence of the increased number of degrees of freedom, when using more complicated models.

Comparison of Solution Side-Chain Conformations with X-ray Data. In solution, the preferred rotameric states of the valine side chains in RNase T_1 adopt χ_1 angles near 180° (Val16, Val67, Val79, and Val89) and near –60° (Val33, Val52, Val78, and Val101), respectively. This is in agreement with a statistical analysis of valine conformations in protein crystals (Janin et al., 1978; McGregor et al., 1987; Ponder & Richards, 1987). According to these analyses, the rotamer with $\chi_1 = +60°$ is less populated than the other staggered states. For steric reasons, a $\chi_1 = +60°$ conformation is energetically unfavorable.

Table 5: Valine Side-Chain Conformations in the X-ray Structure of RNase T_1[a]

residue	χ_1 (deg)	B factors (Å^2) Cα	Cβ	Cγ1	Cγ2	solvent accessibility[b]
Val16	169	7.27	7.70	9.73	12.11	
Val33	–66	10.18	12.68	16.67	11.36	S
Val52	104	22.65	25.53	18.79	22.89	S
Val67	162	9.31	13.07	18.45	16.90	S
Val78	50% 161	5.94	12.12	22.45	5.29	
	50% 45			5.91	21.57	
Val79	176	6.66	8.90	12.73	12.61	
Val89	181	8.41	8.58	9.43	11.58	
Val101	–66	7.88	9.94	12.12	12.44	S

[a] Martinez-Oyanedel et al., 1991. [b] Calculated with the Connolly algorithm (Connolly, 1983).

RNase T_1 contains an α-helix and is folded mainly into β-sheets connected by loop regions. Val16 is located in the α-helical region, while Val78, Val79, Val89, and Val101 form part of the β-sheet. Val33, Val52, and Val67 occur in loop regions and are solvent accessible (Table 5). With respect to the conformational flexibility, a particular correlation with the secondary structure cannot be deduced. The side chains of Val16, Val67, Val79, and Val101 are restricted to a single conformation, while Val52 and Val89 fluctuate around a mean χ_1 angle. The side-chain conformations of Val33 and Val78 represent equilibria between different rotamers. Remarkably, only Val33 is solvent accessible, while the side chain of Val78 is buried in the core of the protein. Thus, a more rigid conformation would have been expected for this residue. It should be mentioned that in all RNase T_1 species with an empty ribose binding site examined so far, Val78 is disordered (Lenz et al., 1993), whereas in protein–ligand complexes in which the ribose binding site is occupied, Val78 maintains one distinct rotamer conformation.

The valine dihedral angles χ_1 found in the X-ray structure of RNase T_1 (Martinez-Oyanedel et al., 1991) are listed in Table 5. With the exception of Val78, the valine side chains adopt rigid conformations in the crystal. Comparing X-ray with NMR data, it is evident that the conformations in the crystal and the predominant rotamers in solution are very similar, albeit the solution structure exhibits more conformational mobility. The more mobile side chains of Val52, Val78, and Val89 may serve as examples for the subtle differences revealed by a detailed comparison.

For Val89, the observed conformational flexibility is not reproduced by the X-ray data. The temperature factors reported are on the order of 10 Å^2 and are thus too low to indicate rotational flexibility.

In solution, we find an approximate 1:3:1 equilibrium of the staggered rotamers I, II, and III for Val78 (Figure 8b) even with both sets of Karplus parameters. The predominant rotamer in solution exhibits a χ_1 angle of –60° irrespective of the model approach used. The X-ray results indicate a two-state conformational equilibrium between conformation 1 with $\chi_1^{(1)} = 161°$ and conformation 2 with $\chi_1^{(2)} = 45°$ (Figure 8a). As indicated in Figure 8a, $C_{\gamma 1}^{(1)}$ in the X-ray conformation (1) ($\chi_1 = 161°$) and $C_{\gamma 2}^{(2)}$ in the X-ray conformation (2) ($\chi_1 = 45°$) have the same coordinates and rather high B factors of 22 Å^2. The calculated electron density for this position from the NMR analysis is 0.4 (19% $C_{\gamma 1}^{(I)}$ + 15% $C_{\gamma 2}^{(III)}$) instead of 0.5 + 0.5 in the X-ray structure. For

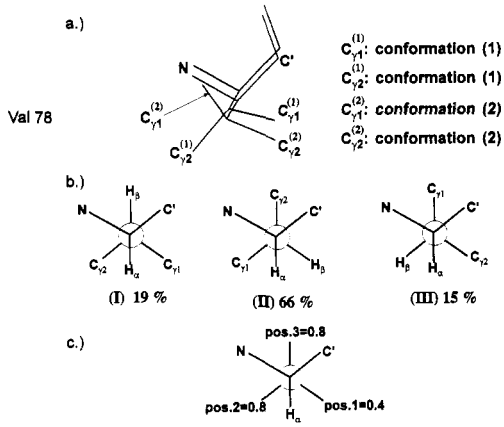

FIGURE 8: Comparison of the X-ray crystal structure and NMR solution structure of Val78 in ribonuclease T_1. (a) X-ray structure: In the X-ray analysis, two equally populated rotamers 1 and 2 with χ_1 angles of 45° and 161° are described. The coordinates and the *B* factors are taken from Martinez-Oyanedel et al. (1991) as deposited in the Brookhaven Protein Data Base. (b) NMR structure: According to model C, a 19% to 66% to 15% equilibrium between the three staggered rotamers I, II, and III is found. For further explanation see text. (c) Electron density for the three positions as calculated from model C.

the other two positions, the electron density from the NMR analysis is 0.8. Scaling of the X-ray *B* factors with the electron densities found in the NMR analysis according to

$$B_{\text{pos.1}} = (0.4/1.0)22\ \text{Å}^2 = 8.8\ \text{Å}^2 \quad (18)$$

$$B_{\text{pos.2}} = (0.8/0.5)5.3\ \text{Å}^2 = 8.8\ \text{Å}^2 \quad (19)$$

$$B_{\text{pos.3}} = (0.8/0.5)5.9\ \text{Å}^2 = 9.4\ \text{Å}^2 \quad (20)$$

yields uniform temperature factors for all three atomic positions. Equal *B* factors and plausible electron densities are expected for a dynamic equilibrium between the *three* staggered rotamers. Therefore, the NMR model is in agreement with the X-ray data, albeit not with the crystallographic χ_1 values. However, there is a correlation between the solution and the crystal side-chain conformation regarding the considerable rotational flexibility observed for this residue.

The conformation of Val52 in solution, as determined from our analysis of ^3J coupling constants, exhibits the most prominent difference to the conformation determined by X-ray crystallography. Contrary to the eclipsed rotamer state (χ_1 = 103°) reported for the crystal structure, we have found a mean χ_1 angle of −37° (Figure 9b). The broad Gaussian distribution (σ = 16°), resulting from the first set of Karplus parameters, indicates a considerable rotational mobility for the side chain, in accord with the location of Val52 in a loop region and with its solvent accessibility. However, a 26% to 74% equilibrium of staggered rotamers I and II, as indicated in Figure 9c, is also in agreement with the ^3J coupling data. In the X-ray structure an eclipsed conformation is found with a bond angle of 127° between $C_{\gamma1}$, C_β, $C_{\gamma2}$ (Figure 9a). The corresponding electron density might be explained as a dynamic equilibrium between the two distinct sites described in the solution conformation (U. Heinemann & W. Saenger, private communication). In the X-ray structure $C_{\gamma1}$ is found eclipsed to C′. N maintains a dihedral angle to $C_{\gamma2}$ of −106°. Assuming the same averaging process in the crystal as in solution, the X-ray electron density can be explained because the site antiperiplanar to C′ is always occupied by a methyl group. The two synclinal sites are occupied either by C_γ or by H_β.

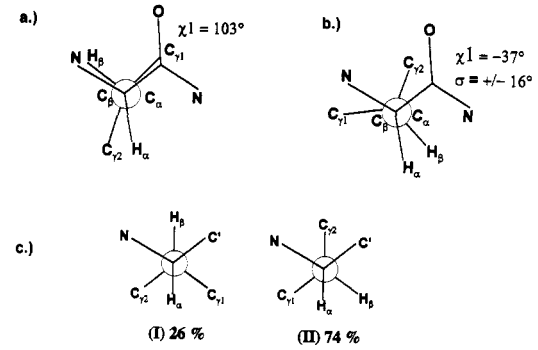

FIGURE 9: Comparison of the X-ray crystal structure and NMR solution structure of Val52 in ribonuclease T_1. (a) X-ray structure: The χ_1 angle of Val52 is 103°, the bond angle $C_{\gamma1}$, C_β, $C_{\gamma2}$ is 127°. Coordinates are taken from the Brookhaven Protein Data Base. Hydrogen postions were calculated according to standard geometries. (b) NMR structure: According to model B, the χ_1 angle of Val52 is −37° with a normal distribution in the range of ±16°. (c) NMR structure: According to model C, an 26% to 74% equilibrium between rotamer I and II is found.

The average electron density therefore appears in between these two sites, namely synperiplanar to C′.

The results of this study are in agreement with the previously reported analysis of homonuclear coupling constants of hen egg white lysozyme (Smith et al., 1991), according to which the rotational flexibility of side chains is not accurately represented by crystallographic χ_1 values.

CONCLUSIONS

Using multidimensional heteronuclear NMR techniques, the vicinal coupling constants $^3J_{H\alpha H\beta}$, $^3J_{C'H\beta}$, $^3J_{NH\beta}$, $^3J_{H\alpha C\gamma1}$, $^3J_{H\alpha C\gamma2}$, $^3J_{C'C\gamma1}$, and $^3J_{C'C\gamma2}$, associated with the torsion angle χ_1 of the valine residues in RNase T_1, were determined. Various models were applied to quantitatively interpret experimental data in terms of χ_1 rotamers. Single-rotamer models, which completely neglect motional effects, were found insufficient to generally explain the experimental coupling constants. Rotational disorder was eventually considered applying Gaussian distributions in χ_1 as well as the staggered-rotamer model. The latter approaches were suitable to characterize side-chain conformational states with respect to small fluctuations about an average χ_1 value and with respect to multiple discrete conformations. Nonstaggered conformers that fit the measured coupling constants were in most instances found to be within ±30° deviation from a staggered conformation.

Three sources of uncertainty turned out to be decisive in determining solution side-chain conformations from an analysis of vicinal coupling constants. The precision in the derived χ_1 angles depends (i) on systematic errors in the ^3J coupling constants originating from nonideal performance of the NMR experiments, (ii) on the accuracy of the empirically calibrated Karplus parameters needed for calculating theoretical ^3J values, and (iii) on the simplifications in the conformational models. In particular, a decision on the validity of a three-site jump model and a rotational-diffusion model cannot be made from the available coupling constant data. The present analysis is only a first step for the investigation of conformational equilibria in proteins. Exhaustive evaluations of vicinal coupling constants for all amino acid side chains are necessary to describe the solution structure of a protein in detail.

ACKNOWLEDGMENT

The authors thank H. Thüring for preparing labeled RNase T_1 and M. Sattler, F. Löhr, and O. Ohlenschläger for helpful

discussions. We thank U. Heinemann and W. Saenger for stimulating discussions comparing NMR with X-ray data.

REFERENCES

Bax, A., Ikura, M., Kay, L. E., & Zhu, G. (1991) *J. Magn. Reson. 91*, 174–178.

Bystrov, V. F. (1976) *Prog. NMR Spectrosc. 10*, 41–81.

Clifford, A. A. (1973) *A Handbook of Multivariate Error Analysis*, pp 71ff, Applied Science Publishers Ltd., London.

Clore, G. M., Driscoll, P. C., Wingfield, P. T., & Gronenborn, A. (1990) *Biochemistry 29*, 7387–7401.

Connolly, M. (1983) *Science 221*, 709–713.

DeMarco, A., & Llinás, M. (1979) *Biochemistry 18*, 3846–3854.

DeMarco, A., Llinás, M., & Wüthrich, K. (1978a) *Biopolymers 17*, 617–636.

DeMarco, A., Llinás, M., & Wüthrich, K. (1978b) *Biopolymers 17*, 2727–2742.

Dzakula, Z., Westler, W. M., Edison, A., & Markley, J. (1992a) *J. Am. Chem. Soc. 114*, 6195–6199.

Dzakula, Z., Edison, A., Westler, W. M., & Markley, J. (1992b) *J. Am. Chem. Soc. 114*, 6200–6207.

Eggenberger, U., Karimi-Nejad, Y., Thüring, H., Rüterjans, H., & Griesinger, C. (1992a) *J. Biomol. NMR 2*, 583–590.

Eggenberger, U., Schmidt, P., Sattler, M., Glaser, S. J., & Griesinger, C. (1992b) *J. Magn. Reson. 100*, 604–610.

Fischman, A. J., Live, D. H., Wyssbrod, H. R., Agosta, W. C., & Cowburn, D. (1980) *J. Am. Chem. Soc. 102*, 2533–2539.

Gelin, B. R., & Karplus, M. (1979) *Biochemistry 18*, 1256–1268.

Griesinger, C., & Eggenberger, U. (1992) *J. Magn. Reson. 97*, 426–434.

Griesinger, C., Sørensen, O. W., & Ernst, R. R. (1985) *J. Am. Chem. Soc. 107*, 6394–6396.

Griesinger, C., Sørensen, O. W., & Ernst, R. R. (1986) *J. Chem. Phys. 85*, 6837–6852.

Griesinger, C., Sørensen, O. W., & Ernst, R. R. (1987) *J. Magn. Reson. 75*, 474–492.

Harbison, G. S. (1993) *J. Am. Chem. Soc. 115*, 3026–3027.

Hoch, J. C., Dobson, C. M., & Karplus, M. (1985) *Biochemistry 24*, 3831–3841.

Hoffmann, E., & Rüterjans, H. (1988) *Eur. J. Biochem. 177*, 539–560.

Hyberts, S. G., Märki, W., & Wagner, G. (1987) *Eur. J. Biochem. 164*, 625–635.

Ichiye, T., & Karplus, M. (1987) *Proteins: Structure, Function and Genetics 2*, 236–259.

Janin, J., Wodak, S., Levitt, M., & Maigret, B. (1978) *J. Mol. Biol. 125*, 357–386.

Karimi-Nejad, Y., Pfeiffer, S., Werner, A., Thüring, H., & Rüterjans, H. (1992) presented at the *XV International Conference on Magnetic Resonance in Biological Systems*, Jerusalem.

Karplus, M. (1959) *J. Chem. Phys. 30*, 11–15.

Karplus, M. (1963) *J. Am. Chem. Soc. 85*, 2870–2871.

Kessler, H., Griesinger, C., & Wagner, K. (1987) *J. Am. Chem. Soc. 109*, 6927–6933.

Kessler, H., Griesinger, C., Müller, A., Lautz, J., van Gunsteren, W. F., & Berendsen, H. J. C. (1988) *J. Am. Chem. Soc. 110*, 3393–3396.

Kopple, K. D., Wiley, G. R., & Tauke, R. (1973) *Biopolymers 12*, 627–636.

Lenz, A., Choe, H.-W., Granzin, J., Heinemann, U., & Saenger, W. (1993) *Eur. J. Biochem. 211*, 311–316.

Mádi, Z. L., Griesinger, C., & Ernst, R. R. (1990) *J. Am. Chem. Soc. 112*, 2908–2914.

Marion, D., & Wüthrich, K. (1983) *Biochem. Biophys. Res. Commun. 113*, 967–974.

Martinez-Oyanedel, J., Choe, H.-W., Heinemann, U., & Saenger, W. (1991) *J. Mol. Biol. 222*, 335–352.

McGregor, M. J., Islam, S. A., & Sternberg, M. J. E. (1987) *J. Mol. Biol. 198*, 295–310.

Montelione, G. T., Winkler, M. E., Rauenbühler, P., & Wagner, G. (1989) *J. Magn. Reson. 82*, 198–204.

Nagayama, K., & Wüthrich, K. (1981) *Eur. J. Biochem. 115*, 653–657.

Nelder, J. A., & Mead, R. (1965) *Comput. J. 7*, 308–311.

Nicholson, L. K., Kay, L. E., Baldisseri, D. M., Arango, J., Young, P. E., Bax, A., & Torchia, D. (1992) *Biochemistry 31*, 5253–5263.

Norwood, T. J., & Jones, K. (1993) *J. Magn. Reson. A 104*, 106–110.

Pace, C. N., Heinemann, U., Hahn, U., & Saenger, W. (1991) *Angew. Chem. 103*, 351–369.

Pachler, K. G. R. (1963) *Spectrochim. Acta 19*, 2085–2092.

Pachler, K. G. R. (1964) *Spectrochim. Acta 20*, 581–587.

Palmer, A. G., Rance, M., & Wright, P. E. (1991) *J. Am. Chem. Soc. 113*, 4371–4380.

Ponder, J. W., & Richards, F. M. (1987) *J. Mol. Biol. 193*, 775–791.

Pople, J. A. (1958) *Mol. Phys. 1*, 3–8.

Press, W. H., Flannery, B. P., Teukolsky, S. A., & Vetterling, W. T. (1989) *Numerical Recipes*, Cambridge University Press, Cambridge.

Quaas, R., McKeown, Y., Stanssens, P., Frank, R., Blöcker, H., & Hahn, U. (1988a) *Eur. J. Biochem. 173*, 617–622.

Quaas, R., Grunert, H.-P., Kimura, M., & Hahn, U. (1988b) *Nucleosides Nucleotides 7*, 619–623.

Richarz, R., Nagayama, K., & Wüthrich, K. (1980) *Biochemistry 19*, 5189–5196.

Sattler, M., Schwalbe, H., & Griesinger, C. (1992) *J. Am. Chem. Soc. 114*, 1126–1127.

Schmidt, J. M., Thüring, H., Werner, A., Rüterjans, H., Quaas, R., & Hahn, U. (1991) *Eur. J. Biochem. 197*, 643–653.

Schwalbe, H., Rexroth, A., Eggenberger, U., Geppert, T., & Griesinger, C. (1993) *J. Am. Chem. Soc.* (in press).

Smith, J. L., Hendrickson, W. A., Honzatko, R. B., & Sheriff, S. (1986) *Biochemistry 25*, 5018–5027.

Smith, L. J., Sutcliffe, M. J., Redfield, C., & Dobson, C. M. (1991) *Biochemistry 30*, 986–996.

Sørensen, O. W. (1990) *J. Magn. Reson. 90*, 433–438.

States, D. J., Haberkorn, X., & Ruben, D. J. (1982) *J. Magn. Reson. 48*, 286–292.

Torda, A. E., Brunne, R. M., Huber, T., Kessler, H., & van Gunsteren, W. F. (1993) *J. Biomol. NMR 3*, 55–66.

Wagner, G., Schmieder, P., & Thanabal, V. (1991) *J. Magn. Reson. 93*, 436–440.

Wasylishen, R., & Schaefer, T. (1972) *Can. J. Chem. 50*, 2710–2712.

Wider, G., Neri, D., Otting, G., & Wüthrich, K. (1989) *J. Magn. Reson. 85*, 426–431.

Zhu, G., & Bax, A. (1990) *J. Magn. Reson. 90*, 405–410.